Article

A Preliminary Analysis of Wind Retrieval, Based on GF-3 Wave Mode Data

Lei Wang [1,2,3], Bing Han [1,2,*], Xinzhe Yuan [4], Bin Lei [1,2], Chibiao Ding [1,2,3,5], Yulin Yao [6], Qi Chen [6]

[1] Key Laboratory of Technology in Geo-Spatial Information Processing and Application Systems, Institute of Electronics, Chinese Academy of Sciences, Beijing 100190, China; wanglei162@mails.ucas.edu.cn (L.W.); leibin@mail.ie.ac.cn (B.L.); cbding@mail.ie.ac.cn (C.D.);
[2] Institute of Electronics, Chinese Academy of Sciences, Beijing 100190, China;
[3] School of Electronic, Electrical and Communication Engineering, University of Chinese Academy of Sciences, Beijing 100049, China
[4] National Satellite Ocean Application Service, State Oceanic Administration, Beijing 100081, China; harley_yuan@mail.nsoas.org.cn
[5] National Key Laboratory of Microwave Imaging Technology, Institute of Electronics, Chinese Academy of Sciences, Beijing 100190, China
[6] China Centre for Resource Satellite Data and Application, Beijing 100094, China; yaoyulin886@163.com (Y.Y.), chenq_cn@163.com (Q.C.);
[*] Correspondence: han_bing@mail.ie.ac.cn; Tel.: +86-10-5888-7208 (ext. 8956)

Abstract: This paper gives an analysis of measurements of the normalized radar cross-section(NRCS) in Wave Mode for Chinese C-band Gaofen-3(GF-3) synthetic aperture radar (SAR). Based on 2779 images from GF-3 quad-polarization SAR in Wave Mode and collocated wind vectors from ERA-Interim, this experiment verifies the feasibility of using ocean surface wind fields and VV-polarized NRCS to perform normalized calibration. The method uses well-validated empirical C-band geophysical model function (CMOD4) to estimate the calibration constant for each beam. In addition, the relationship between cross-pol NRCS and wind vectors is discussed. The cross-pol NRCS increases linearly with wind speed and it is obviously modulated by the wind direction when the wind speed is greater than 8m/s. Furthermore, the properties of the polarization ratio, denoted PR, are also investigated. The PR is dependent on incidence angle and azimuth angle. Two empirical models of the PR are fitted, one as a function of incidence angle only, the other with additional dependence on azimuth angle. Assessments show that the σ_{VV}^0 retrieved from new PR models as well as σ_{HH}^0 is in good agreement with σ_{VV}^0 extracted from SAR images directly.

Keywords: Gaofen-3; SAR; Wave Mode; calibration constants; cross-pol; noise floor; polarization ratio;

1. Introduction

With the continuous depletion of global petroleum energy, the development and utilization of clean wind energy have become a hot topic in recent decades. Offshore wind energy has been focused by researchers due to the vast area of marine resources. Measurements of offshore wind information also contribute to oil spill monitoring, weather forecasting and understanding of air-sea interactions [1-3]. Spaceborne active microwave scatterometer such as QuickSCAT and ASCAT have provided mature wind products for National Oceanic and Atmospheric Administration(NOAA) [4,5]. However, the wind fields acquired by scatterometer cannot be applied to fine scale marine products due to the course spatial resolution (12.5km~25km) [6]. Because of feasures like imaging at all-weather conditions and high spatial resolution, synthetic aperture radar (SAR) has been widely used in military, economics, and science, and plays an important role in the retrieval of ocean surface wind fields, especially for C-band (~5.3GHz) SAR [7].

Numerous studies have revealed that ocean surface normalized radar cross-section (NRCS) obtained from C-band SAR is mainly dominated by resonant Bragg backscattering at the wavelength of centimeter scale [8-10]. This scale roughness is predominantly influenced by local wind and

therefore ocean wind information may be extracted from SAR images [11]. In recent decades, several empirical geophysical model functions (GMFs), such as CMOD4 [12], CMOD_IFR2 [13], CMOD5 [14] and CMOD5.N [15] have been proposed to perform ocean surface wind retrieval. These GMFs relate the NRCS to the incidence angle, wind speed at a height of 10m above sea level, and azimuth angle (radar look angle with respect to wind direction). Not only scatterometer, such as QuickSCAT [16,17] and ASCAT [18], they can also accurately retrieve the wind speed from SAR images (within about 2m/s), e.g., ENVISAT [19], RADARSAT-1/2 [20-22] and Sentinel-1A/B [23]. However, such GMFs are only suitable for VV-polarized NRCS, no similar models exist to retrieve wind speed from images in HH-polarization. Therefore, it is necessary to convert HH-polarized NRCS to VV-polarization using polarization ratio (PR), denoted as $PR = \sigma_0^{VV}/\sigma_0^{HH}$ [linear units], before retrieving wind speed [24-28]. In traditional research, it is generally believed that the PR is only relevant to incidence angle [24]. Recent studies in [27,28] show that the PR is also dependent on speed and azimuth. These results reveal that different satellites have their own optimal PR and GMF. Thus, the choice of suitable hybrid model is critical for Gaofen-3 satellite [29].

Recent decades, wind speed retrieval from cross polarized (cross-pol) NRCS has become to a focus due to the saturation of co-pol data at high wind speed. Some studies of cross-pol images have been conducted for RADARSAT-1/2 quad-polarization and dual-polarization [32-37]. Hwang and Zhang et al. [30,31] reveal the breaking contribution of cross-pol NRCS and emphasize the advantages of wind retrieval with cross-pol data at high wind speeds. Vachon and Zhang et al. [32,33] propose a cross-pol wind retrieval model which is only relevant to wind speed and independent on incidence angle as well as wind direction, respectively. In [34-36], Hwang and Shen propose that the VH NRCS of RADARSAT-2 dual-polarization mode is also relevant to incidence angle and the noise floor must be considered before wind retrieval. Moreover, Huang et al. [38] conduct an evaluation on cross-pol NRCS in Sentinel-1 IW mode and propose a wind retrieval algorithm related to incidence angle and wind direction. The above studies show that the cross-pol NRCS has potential to retrieve high wind speeds, e.g. hurricanes and typhoons.

The accuracy of the retrieved wind vector is strongly affected by the absolute radiometric calibration accuracy of NRCS. Accurate wind speed can be obtained from refined NRCS. Therefore, it is possible to assess the accuracy of the calibration by using GMFs and known wind information. Horstmann et al. [39] propose a method for estimating ERS SAR calibration constants using C-band models and ocean surface wind fields. Stoffelen et al. [40] obtain an accurate calibration of a scatterometer over the ocean using CMOD4 and wind fields from European Centre for Medium-Range Weather Forecasts (ECMWF). This method achieves a calibration accuracy of 0.1 dB. Verspeek et al. [41] propose an estimating correction table based on CMOD5.N to improve ASCAT wind retrieval. Zhu et al. [42] use Numerical Ocean Calibration (NOC) to calibrate HY-2 SCAT and the retrieved winds are in good agreement in winds from ECMWF.

The Gaofen-3 (GF-3) satellite which was launched on 10 August 2016 by the China Academy of Space Technology (CAST) is the first C-band multi-polarization SAR with the highest resolution of 1m in China. It has characteristics such as high resolution, large coverage, long-life operation and multiple imaging modes, including Wave Mode [43]. To date, some preliminary evaluations of ocean application have been carried out. Shao et al. [44] collect 244 Stander Stripmap (SS) and Quad-Polarization Stripmap (QPSI and QPSII) mode images to complete wind and wave retrieval firstly. In [29], Wang et al. validate the GF-3-derived winds against NDBC measurements using SS, QPSI, QPSII, FSI and NSC mode data. Ren et al. [45] conduct a comprehensive analysis of QPSI and QPSII mode data in each polarization. Several empirical algorithms for significant wave height in Wave Mode data and wind retrieval from cross-polarization in typhoons are also discussed in [46,47], which uses GF-3 images acquired in Global Observation (GLO) and Wide ScanSAR (WSC) mode.

The remainder of this paper is organized as follows. Section 2 describes the GF-3 Wave Mode SAR images and other validated data, including ECMWF ERA-Interim re-analysis wind fields and Amazon rainforest images. Methodologies for correcting calibration constants, fitting PR models and cross-pol wind speed retrieval formula are introduced in section 3. Section 4 shows results of

calibration, polarization conversion and wind speed retrieval accuracy. Finally, discussion and conclusion are presented in section 5 and 6.

2. Description of Datasets

2.1. GF-3 SAR Wave Mode images

An experiment in [48] shows that GF-3 images can meet the satellites' polarimetric accuracy requirements, and the channel imbalance is 0.5dB as well as a crosstalk accuracy of -35dB. In this study, 6355 GF-3 Level-1A Wave Mode images are collected between March 1, 2017 and December 31, 2017 over the Pacific, Atlantic and Indian Ocean. The task of Wave Mode is to observe ocean surface waves over open ocean, and the size of Wave Mode image is about 5km × 5km every 50 km along the orbit. Incidence angle is the predominant difference between Wave Mode and other modes. Although the incidence angle of Wave Mode ranges from 20° to 50°, it only fixes in 28 beams with a narrow data acquisition window about 0.4°. This results in discrete incidence angle for images between different beams, e.g. incidence angle of beam 189 is about $21.5 \pm 0.2°$ and the incidence angle of beam 190 is about $23.7 \pm 0.2°$ etc. [46,43]. The parameter details of Wave Mode products are listed in Table 1 and the time distribution of data in each ocean is listed in Table 2.

Table 1. Parameters for GF-3 Wave Mode.

Imaging mode	Incidence angle (°)	Polarization	Resolution (m)	Swath (km)
WAV	20-50	HH+VV+HV+VH	10	5

Table 2. Time Distribution of SAR Images in Each Ocean

Oceans	Pacific	Atlantic	Indian
Distribution	Mar、Apr、Sep、Oct、Nov、Dec	Apr、May、Jun	Mar、April

The Level-1A products are single look complex (SLC) images. Let I represents real channel of images, Q as the imaginary channel. The equation of NRCS is as follow.

$$\sigma^0 = 10 * log\left[\left(\frac{I}{32767} * Qualify\right)^2 + \left(\frac{Q}{32767} * Qualify\right)^2\right] - K\_const \quad (1)$$

Where σ^0 is the NRCS in dB, Qualify is the QualifyValue in product description xml of GF-3, and K_const is the calibration constant.

Several studies indicate that wind speed can only be retrieved from pure ocean SAR images which are free of sea features not due to the local wind, e.g. ice and slicks [2,49]. To screen out the Wave Mode images which are not affected by features due to slicks or ocean phenomenon, the homogeneity check procedure proposed in [46] is used before the experimental study. Wang et al. [46] show that the Wave Mode normalized variance (*cvar_vv*) computed from VV-polarization images can be used as a standard for verifying image homogeneity. Here, we also choose the images which with $1.1 < cvar\_vv < 1.6$ for developing and validating wind retrieval algorithms. The parameter of homogeneity test is defined as

$$cvar\_vv = var\left(\frac{I-\bar{I}}{\bar{I}}\right) \quad (2)$$

where $\bar{I}$ is the mean intensity of GF-3 Wave Mode image in VV-polarization. In addition, inappropriate receiver gain setting causes too high energy input to the ADC converter and may lead to saturation of output power [49]. It greatly affects the experimental results. Hence, this experiment only selects SAR images with 0% saturation coefficient which is provided in product description xml.

After the above two preprocessing processes, a total of 4690 GF-3 Wave Mode images are selected from 6355 images. The result shows that the small incidence angle (in-angle < 36°) co-pol data is almost saturated, according to product description xml. Therefore, the analyzed incidence angle of this paper is only from 39° to 47°. The detail information of data distribution is shown in the Figures 1-3 below. To guarantee the validity of experiment, this experiment divides the whole data

Peer-reviewed version available at Sensors 2018, 18, 1604; doi:10.3390/s18051604

into training and testing set randomly first. Then, a small amount of data is adjusted artificially so that both sets can cover full range of incidence angles, azimuth angles and wind speeds. Finally, 2779 match-ups are chosen as training set and other 1911 samples as testing set.

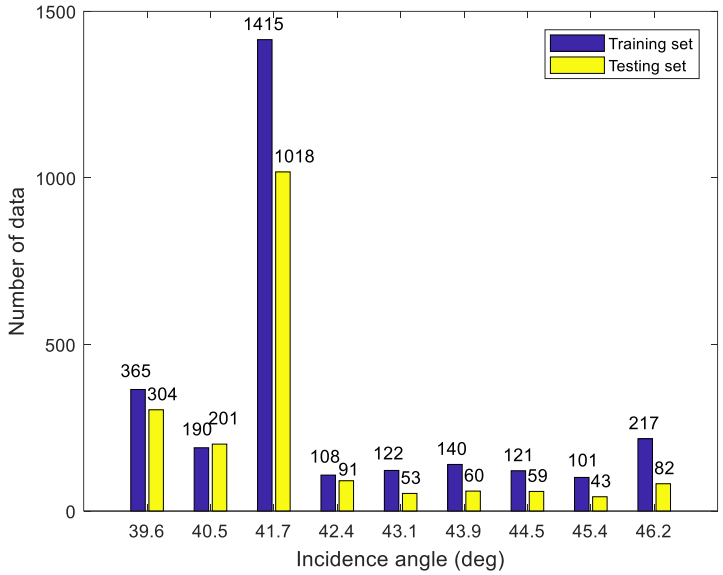

Figure 1. Incidence angle histogram of the data set

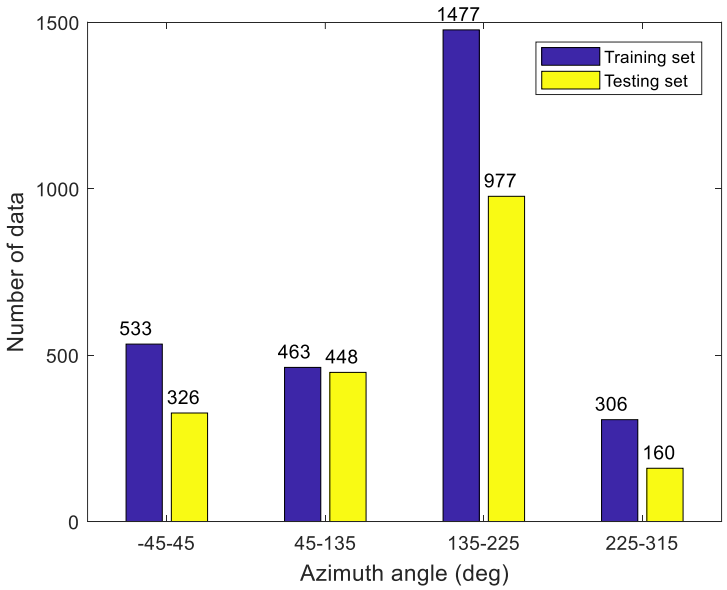

Figure 2. Azimuth angle histogram of the data set

Preprints (www.preprints.org) | NOT PEER-REVIEWED | Posted: 9 May 2018 doi:10.20944/preprints201804.0223.v2

Peer-reviewed version available at Sensors 2018, 18, 1604; doi:10.3390/s18051604

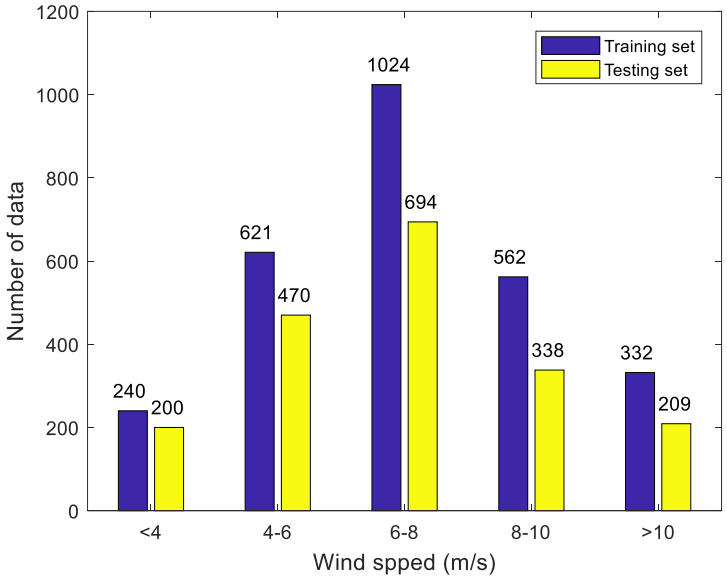

Figure 3. Wind speed histogram of the data set

2.2. Other Validation Sources

ERA-Interim is a global atmospheric re-analysis from 1979, continuously updated in real time, provided by ECMWF which is an independent intergovernmental organization supported by 34 states. The re-analysis wind field data is widely used in retrieval and comparison of wind vectors [12-15]. In this study, the spatial resolution of wind products downloaded on [50] is 0.125°×0.125° (lat/lon), and the temporal resolution is 6h (00:00, 06:00, 12:00, 18:00).

The Amazon rainforest has excellent temporal and spatial stability as a radar distributed target calibration source. And its maximum backscatter deviation is about 0.2dB [51]. There have been numerous researches using the Amazon rainforest for radar radiometric calibration [52]. Here, this experiment uses beam 205 SAR images which have a large number of data and the Amazon rain forest Wave Mode SAR images of corresponding beam to validate the feasibility of ocean calibration.

3. Experiments and Analysis

For the 2779 training data and 1911 testing data, a 512 × 512 pixel boxcar is used in each center of Wave Mode images to average the NRCS in co-polarization (HH and VV), so that the NRCS spacing is about 5km. As mentioned in section 2, the wind fields' spatial resolution is about 12.5km × 12.5km. To improve the match accuracy between wind fields and SAR images, we interpolate the wind fields time to 1h using a cubic spline interpolation and use bilinear interpolation to interpolate four velocity components near the center point to the center. And the time difference between SAR image and wind vector is within 30min.

3.1. Calibration Method Based on Ocean Wind

As shown in equation (1), the NRCS in dB is linear with the calibration constant. It provides a possibility for using the wind fields and GMFs to retrieve the calibration constant. In [53], it is found that CMOD4 has a better performance than CMOD5 under low to moderate wind speed. The wind speed range used in this paper is mainly focused on low to moderate wind speeds. Therefore, this experiment uses CMOD4 to obtain simulated VV-polarized NRCS. The difference between simulated NRCS and the value extracted directly from the corresponding image is the stimulated calibration constant. This method requires plentiful fitted data to ensure the accuracy of results and each beam has their own calibration constant. Therefore, the match-up data of 41.7° incidence angle (beam 205) in the training set is used to verify the calibration method. To guarantee the reliability of the

Preprints (www.preprints.org) | NOT PEER-REVIEWED | Posted: 9 May 2018 doi:10.20944/preprints201804.0223.v2

Peer-reviewed version available at Sensors 2018, 18, 1604; doi:10.3390/s18051604

calibration method, this experiment only selects data with wind speed higher than 4m/s [39]. Moreover, the distribution of wind speed and direction in the experimental data set also affects the calculation of calibration constant. Hence, we first split the training set into wind speed bins of size 2m/s and azimuth bins of size 90°. Then, let each speed bin has roughly the same amount of data and filter data in each speed bin so that the distribution of azimuth angle is uniform. Finally, 901 uniform match-ups are obtained to implement the calibration method. Figure 4 shows the relationship between simulated NRCS by CMOD4 and values obtained directly from VV polarized images. And the errorbar of bin 2dB is also plotted.

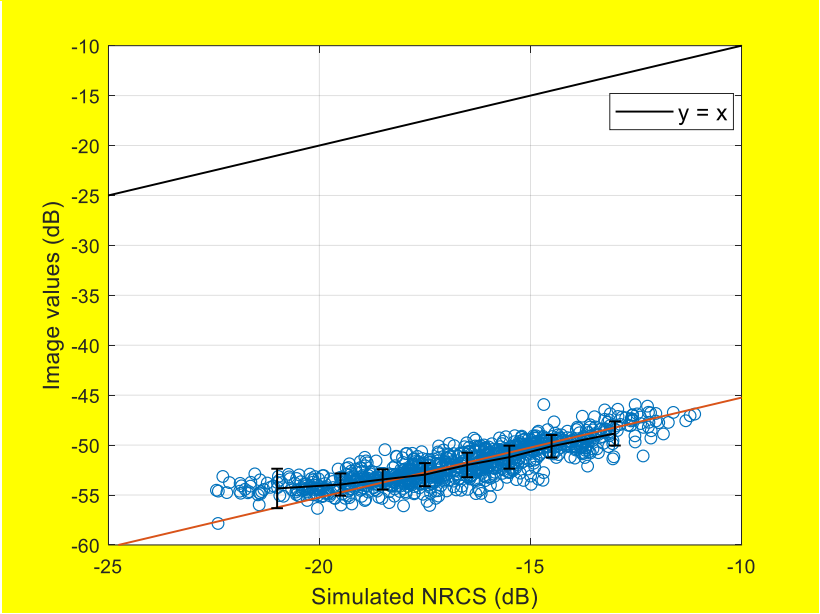

Figure 4. Relationship between simulated NRCS and values obtained directly from images

The solid black line in Figure 4 is the bisector of the axis quadrant and the solid red line is the fitting curve of the training data with the same slope. As shown in the Figure, the difference between the simulated NRCS and image values is a constant. The best calibration constant is calculated using a minimum squared-error criterion. And the calculated calibration constant is 29.486. The calibration constant of beam 205 provided by China Centre for Resources Satellite Data and Application is 29.665. The difference between provided constant and calculated constant is within 0.2dB. It shows the method has a good performance. The obtained calibration constants of each beam are listed in appendix A.

3.2. Analysis of Wind sensitivity for Cross-pol NRCS

The cross-pol backscattering signal-to-noise ratio (SNR) of ocean surface is much weaker than co-pol signal. Therefore, it is necessary to compare cross-pol NRCS with the system noise floor before wind retrieval [36]. The Institute of Electronics, Chinese Academy of Sciences provides a ground system processing technology for GF-3 satellite and can obtain the noise gain coefficient of Wave Mode. Due to the limited number of products with system noise gain coefficient, only 138 sets of beam 205 match-ups with noise floor are collected. Figures 5 (a) and (b) show the HV-polarized NRCS as a function of ERA-Interim re-analysis wind speed and the difference between σ^0_{HV} and σ^0_{HV} which is removed noise floor, respectively.

As illustrated in Figure 5 (a), the HV-polarized noise floor of beam 205 is about -40 dB. It is sufficiently low and the noise performance of GF-3 Wave Mode is better than RADARSAT-2 quad-polarization mode which has the noise floor of -36 dB [45]. Figure 5 (b) shows that the noise floor has some effect on cross-pol signals at low wind speed (< 10 m/s) and the difference between σ^0_{HV} and denoised σ^0_{HV} can be ignored at high wind speed. However, the number and distribution of noise floor is limited in this experiment. The noise floor of different beams may have some differences and

Preprints (www.preprints.org) | NOT PEER-REVIEWED | Posted: 9 May 2018 doi:10.20944/preprints201804.0223.v2

Peer-reviewed version available at Sensors 2018, 18, 1604; doi:10.3390/s18051604

σ^0_{HV} without noise removed also shows a clear linear relationship with wind speed. Therefore, this experiment temporarily ignores the effect of noise floor. The relationship between the NRCS σ^0_{HV} after calibration correction and wind speed is shown in Figure 6. Different colors represent different incidence angles. The errorbar of bin 2m/s is also plotted. As shown in Figure 6, the σ^0_{HV} is independent on incidence angle and exists obvious linear relationship with wind speed. The black solid line is obtained using a non-linear least-squares method, and the formulation is

$$\sigma^0_{HV} = 0.6359 * U_{10} - 36.1384 \quad (3)$$

where σ^0_{HV} is the HV-polarized NRCS in dB and U_{10} is the wind speed at 10m.

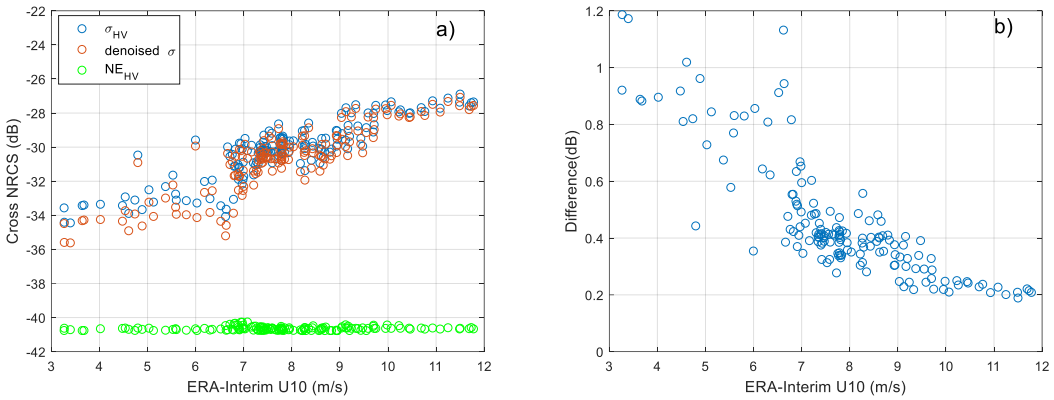

Figure 5. HV-polarized NRCS and noise floor versus wind speed

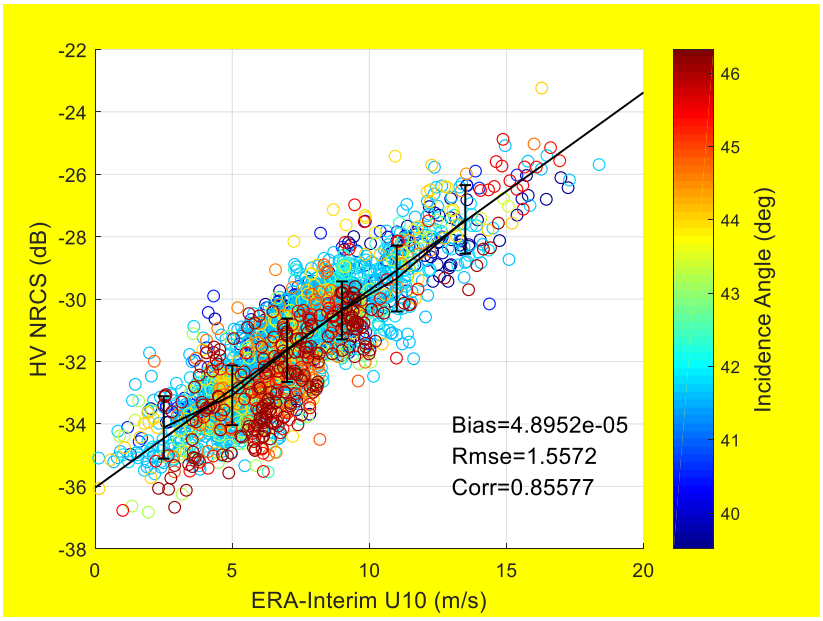

Figure 6. Relationship between NRCS and wind speed (different colors represent different incidence angle)

The wind retrieval algorithm of cross-pol NRCS in this study is similar to the formula in [32,33,45]. The retrieved wind speed using (3) has an RMSE of 1.56 m/s and a correlation coefficient of 0.86. It indicates the accuracy of cross-pol wind retrieval algorithm under low to moderate wind speed, and wind speed can be retrieved directly from cross-pol NRCS without inputting wind direction and incidence angle.

Preprints (www.preprints.org) | NOT PEER-REVIEWED | Posted: 9 May 2018 doi:10.20944/preprints201804.0223.v2

Peer-reviewed version available at Sensors 2018, 18, 1604; doi:10.3390/s18051604

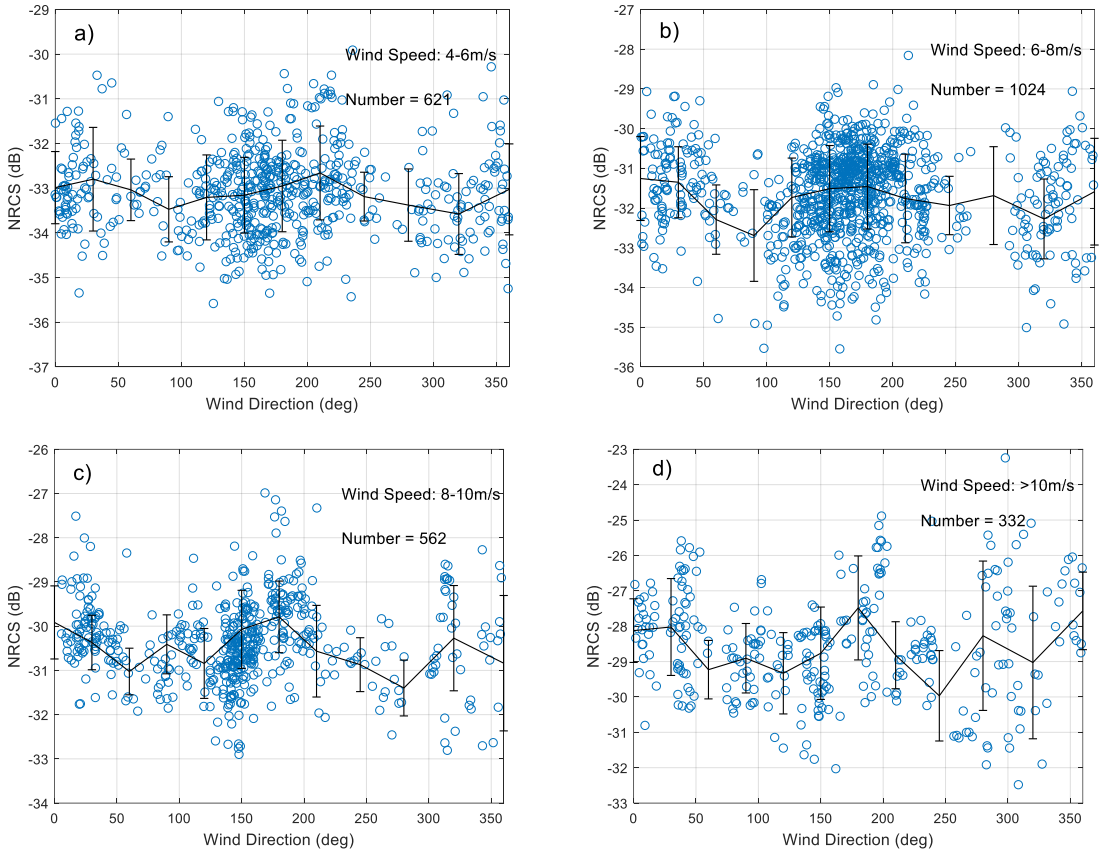

Figure 7. Relationship between cross-pol NRCS and azimuth angle

This paper also assesses the relationship between cross-pol NRCS and azimuth angle at different winds. The training set is divided into 4-6m/s, 6-8m/s, 8-10m/s, >10m/s four sets, respectively, and the variation trend of σ_{HV}^{0} with azimuth angle is shown in Figures 7(a)-(d). Figures 7 also draw the mean value line at each bin 30° with errorbars. When speed is higher than 8m/s, the σ_{HV}^{0} is subject to obvious wind direction modulation and the maximum change is about 2.5dB in different wind directions. This property is consistent with GF-3 QPSI and QPSII mode data in [45]. Therefore, the influence of wind direction should be considered when retrieving high wind speeds, e.g. hurricanes and typhoons.

3.3. Development of PR Models

Figure 8 shows the relationship between PR and incidence angle as well as wind speed based on 2779 training data. Different colors represent the different wind speeds. And the errorbar of each incidence angle bin is also plotted. The PR rises rapidly with increasing incidence angle as previous reports.

Preprints (www.preprints.org) | NOT PEER-REVIEWED | Posted: 9 May 2018 doi:10.20944/preprints201804.0223.v2

Peer-reviewed version available at Sensors 2018, 18, 1604; doi:10.3390/s18051604

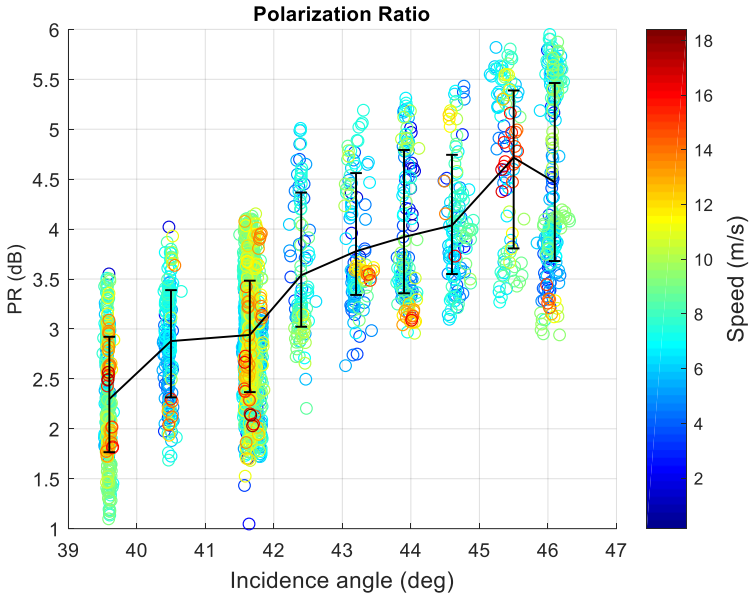

Figure 8. PR as a function of incidence angle (different colors represent different wind speed)

Here, A PR mode which is only related to the incidence angle is first fitted, defined as Model 1. The formula is

$$PR = Aexp(B\theta) + C \quad (3)$$

where PR is in linear unit, and A, B as well as C are coefficients fitted by a nonlinear least squares method. They are given in Table 3.

Table 3. Coefficients of Model 1

Cofficient	Fitted valuses
A	0.02985
B	0.09727
C	0.305

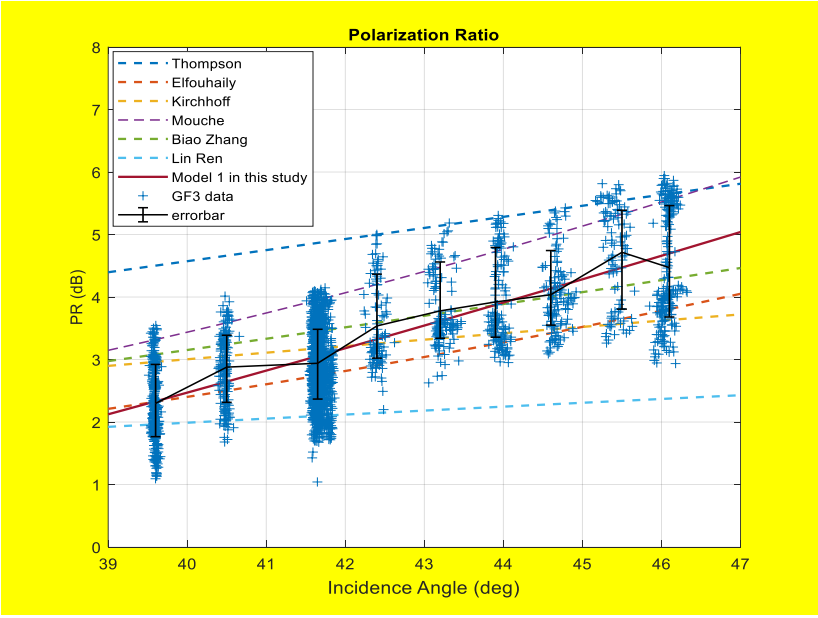

Figure 9. Comparison between Model1 and other PR models

Preprints (www.preprints.org) | NOT PEER-REVIEWED | Posted: 9 May 2018 doi:10.20944/preprints201804.0223.v2

Peer-reviewed version available at Sensors 2018, 18, 1604; doi:10.3390/s18051604

Comparison with other PR models introduced in section 1 is shown in Figure 9. PR models of Biao Zhang and Mouche [27,28] are also an exponential of the incidence angle like the one in present study, however different coefficients are found. The formula of other researchers [24,45] is expressed as

$$PR = (1 + 2tan^2\theta)^2/(1 + \alpha tan^2\theta)^2 \quad (4)$$

where α is an adjustable parameter. As illustrated in Figure 9, the Model 1 is closest to the mean of GF-3 Wave Mode.

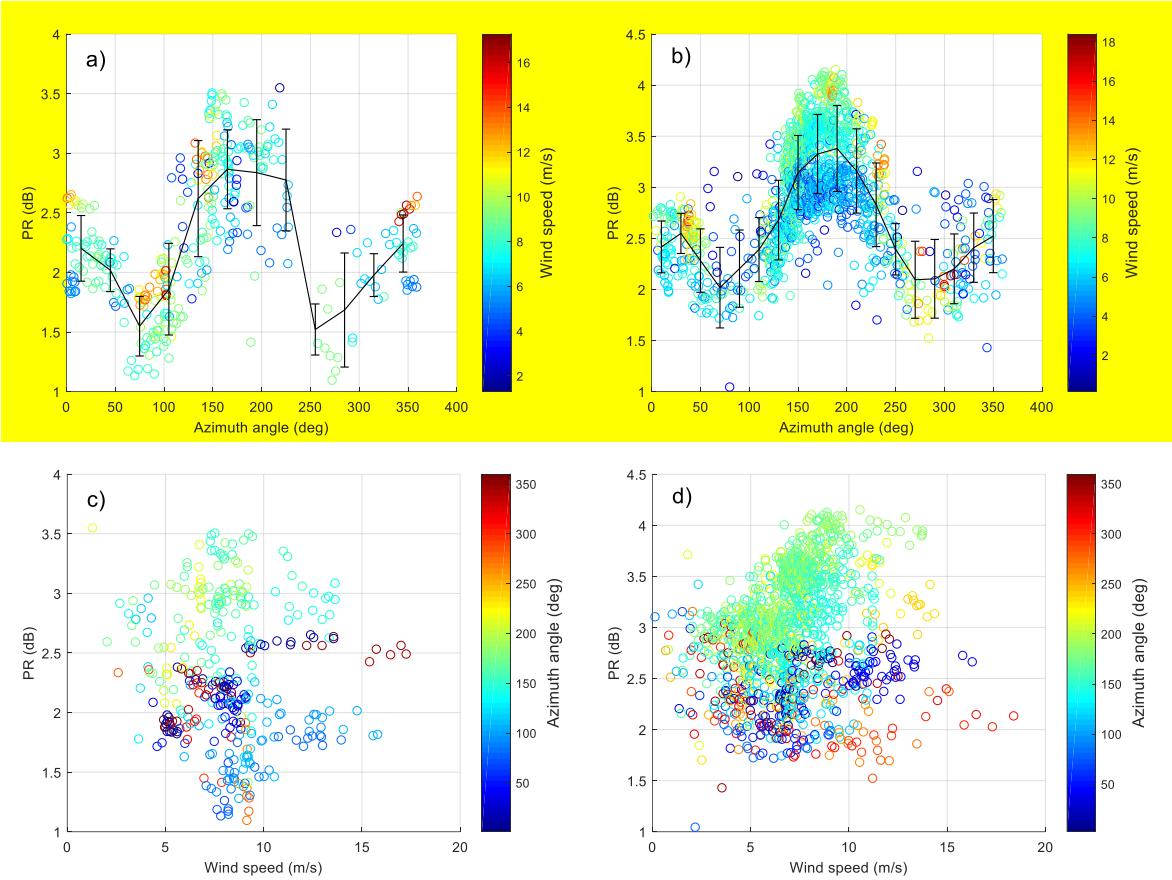

Figure 10. (a) and (b) represent the variation between PR and azimuth angle and different color shows different wind speed. (c) and(d) show the relationship between PR and wind speed. Different color represents different azimuth. (a) and (c) are at incidence angle 39.6°. (b) and (d) are at incidence angle 41.6°.

To give a more comprehensive PR analysis for GF-3 Wave Mode data, the relationship between PR and azimuth angle is also studied. It shows a similar characteristic described in [28]. The variation of PR with azimuth angle and wind speed is shown in Figures 10 (a), (b), (c) and (d) at the incidence angle of 39.6° and 41.7° (beam 202 and 205). The errorbars of bin 30° and 20° are plotted in (a) and (b), respectively. Figures 10 (a) and (b) show that there is an approximate cosine relationship between PR and azimuth angle like the characteristic between NRCS and azimuth angle. The maximum of PR is observed in downwind direction ($\phi = 180°$), a secondary maximum is appeared in upwind direction ($\phi = 0°$) and the minimum values are in crosswind ($\phi = 90°$). This is slightly different from NRCS which appears maximum in upwind and secondary maximum value in downwind. In addition, Figures 10 (c) and (d) show the PR tends to increase with the increase of wind speed (<10m/s) in the downwind, while it is independent with wind speed in other wind direction. To more clearly analyze the variation of PR with wind speed in downwind, this experiment screens out beam 205 data with azimuth angle of $180 \pm 10°$, and the relationship between the PR and wind speed is plotted in Figure 11. The correlation coefficient (0.7572) between PR and wind speed illustrates that the PR is positively related to the wind speed in downwind.

Preprints (www.preprints.org) | NOT PEER-REVIEWED | Posted: 9 May 2018 doi:10.20944/preprints201804.0223.v2

Peer-reviewed version available at Sensors 2018, 18, 1604; doi:10.3390/s18051604

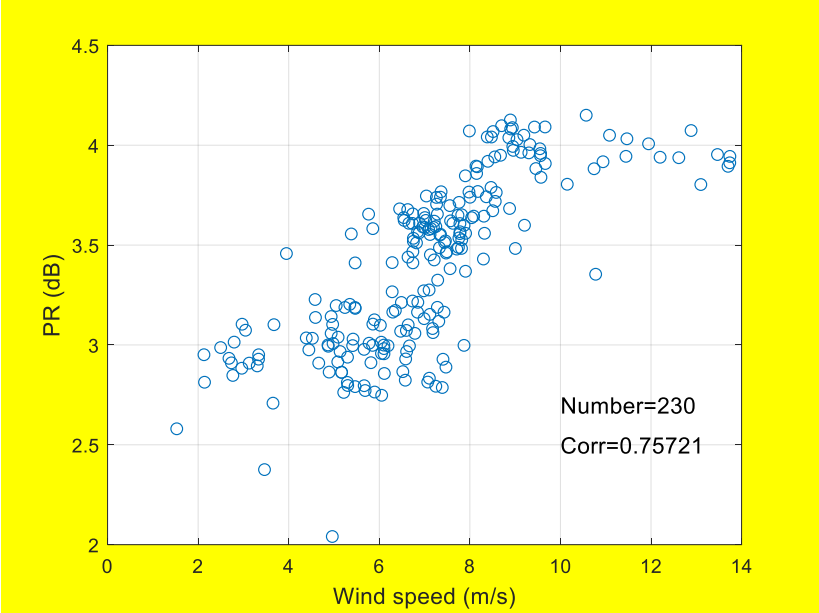

Figure 11. The relationship between PR and wind speed of beam 205 data in downwind

However, it cannot be concluded that the PR increases linearly with wind speed due to insufficient high wind speed data in downwind. Hence, this experiment temporarily ignores the influence of wind speed and fits training set using nonlinear least squares, deriving Model 2 for PR with additional dependence on azimuth angle. The Model 2 is assumed to follow

$$PR(\theta,\phi) = C_0(\theta) + C_1(\theta)\cos\phi + C_2(\theta)\cos 2\phi \quad (5)$$

where ϕ is azimuth angle. In each azimuth angle, the relationship between PR and incidence angle is also defined as exponential function.

$$PR_\phi(\theta) = A_\phi exp(B_\phi\theta) + C_\phi \quad (6)$$

The coefficients C_i(i = 0, 1, 2) can be calculated by the method of undetermined coefficients, and the formulas are as follow

$$C_0(\theta) = \big(PR(\theta,0) + PR(\theta,\pi) + 2PR(\theta,\pi/2)\big)/4 \quad (7a)$$

$$C_1(\theta) = \big(PR(\theta,0) - PR(\theta,\pi)\big)/2 \quad (7b)$$

$$C_2(\theta) = \big(PR(\theta,0) + PR(\theta,\pi) - 2PR(\theta,\pi/2)\big)/4 \quad (7c)$$

First, the coefficients (A_ϕ, B_ϕ, C_ϕ) of three main directions (upwind, downwind, crosswind) are fitted using a nonlinear least squares method. Then using them to obtain coefficients C_i. Table 4 shows the fitting results.

Table 4. Coefficients of Model 2

Coefficients	Fitted values
A_0	0.1715
B_0	0.06242
C_0	-0.4342
$A_{\pi/2}$	0.9331
$B_{\pi/2}$	0.03606
$C_{\pi/2}$	-2.44
A_π	0.000393
B_π	0.1912
C_π	1.119

4. Validation and Results

4.1. Results of Ocean Calibration

Preprints (www.preprints.org) | NOT PEER-REVIEWED | Posted: 9 May 2018 doi:10.20944/preprints201804.0223.v2

Peer-reviewed version available at Sensors 2018, 18, 1604; doi:10.3390/s18051604

The calibration constant provided by China Centre for Resources Satellite Data and Application is derived from system bandwidth and antenna pattern and has not been verified by field calibration. Therefore, 7 GF-3 Wave Mode SAR images of the Amazon rainforest area in beam 205 are collected to verify the calibration constant obtained in section 3.2. The distribution of Amazon rainforest γ is shown in Figure 12.

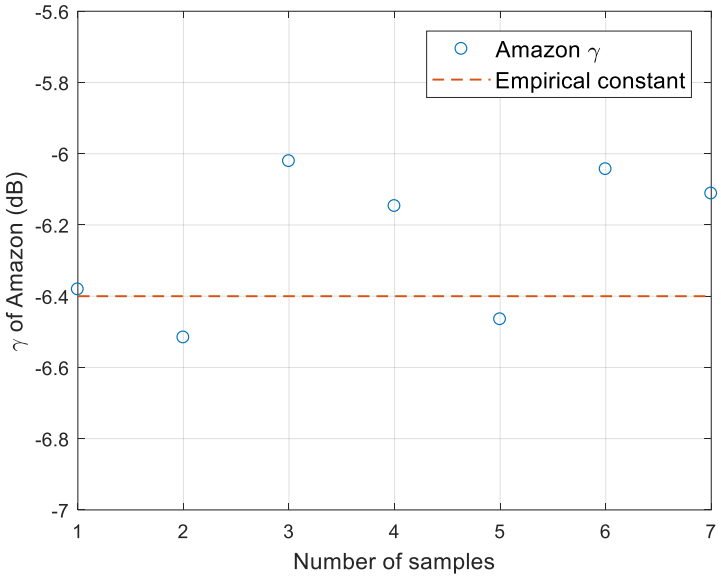

Figure 12. Distribution of Amazon rainforest γ

As described in [52], the γ of Amazon rainforest can be considered as a constant value due to the stability of this area and it is independent on incidence angle. The γ can be characterized as

$$\gamma = \sigma^0/\cos\theta = \beta^0 \tan\theta \quad (8)$$

where γ describes the reflectivity of distributed scatterers per unit area of the incident wave front, σ^0 describes the reflectivity per unit area of horizontal surface and β^0 describes the radar reflectivity per unit pixel area [54]. It is generally accepted that the γ of Amazon rainforest is around -6.4dB. And the distribution of γ from RADARSAT-1 is $-6.47 \pm 0.71dB$ according to [52]. Figure 12 illustrates the γ of GF-3 Wave Mode data in beam 205 is around $-6.4 \pm 0.4dB$. Therefore, it can be demonstrated that the calibration constant calculated using the ocean calibration is accurate. And if enough data can be acquired, the calibration constant can be obtained continuously using the ocean surface wind fields. It provides the possibility for normalized calibration.

Based on the obtained calibration constant, this experiment uses GMFs to perform wind speed retrieval on beam 205 data of testing set. Figures 13 (a)-(d) show the comparison between ERA-Interim wind speeds and retrieved wind speeds using CMOD4, CMOD_IFR2, CMOD5, CMOD5.N , respectively.

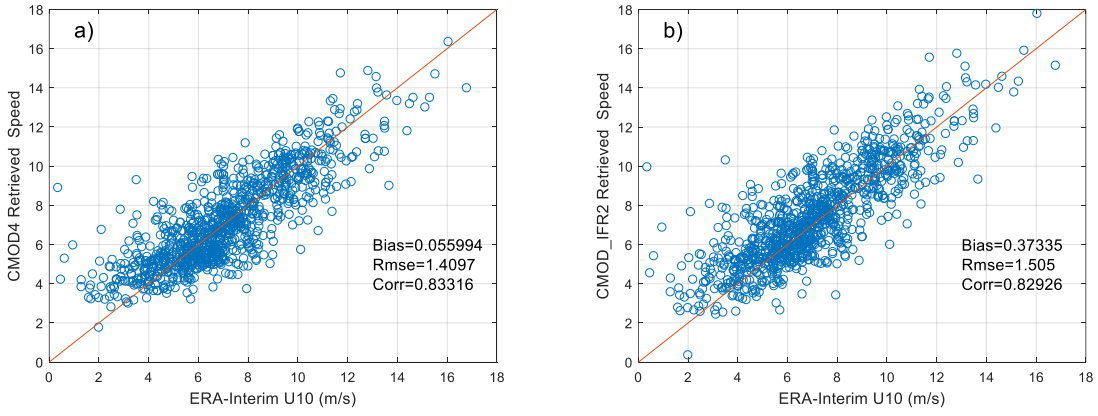

Preprints (www.preprints.org) | NOT PEER-REVIEWED | Posted: 9 May 2018 doi:10.20944/preprints201804.0223.v2

Peer-reviewed version available at Sensors 2018, 18, 1604; doi:10.3390/s18051604

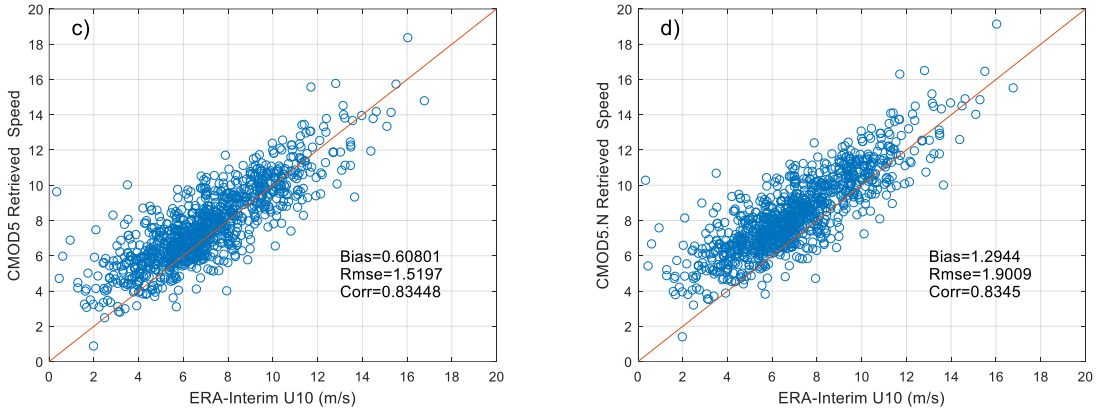

Figure 13. Comparison of ERA-Interim U10 with SAR-derived wind speeds

As demonstrated in Figures 13, the estimated calibration constant can be well applied to SAR image wind speed retrieval and the RMSE of retrieved speed is less than 2m/s. However, large inaccuracies may occur in wind retrieval using GMFs when the wind speed is lower than 2m/s. The accuracy of retrieved speed using CMOD4 is higher than others at low to moderate wind speeds and its RMSE is 1.41m/s. The advantage of CMOD5 cannot be verified due to the lack of data when the wind speed comes to high.

4.2. Validation of Wind Retrieval for Cross-polarization

The testing set is used to evaluate the performance of cross-polarization wind retrieval formula in this paper compared with algorithms in [32,33,45]. The RMSE , bias and R-squares between ERA-Interim U10 and retrieved speed are listed in Table 5.

Table 5. Comparison of Wind Speed Retrieval Algorithm

	Rmse (m/s)	Bias (m/s)	R-squares
Mine	1. 4990	-0.1605	0.6310
Vachon	1.6043	0.2191	0.5773
Zhang	1.6227	-0.0106	0.5675
Ren	2.0371	-1.1586	0.3184

As shown in Table 5, the algorithm fitted in this paper has the optimal inversion accuracy with RMSE 1.499 m/s. The formula proposed by Zhang has the smallest bias with -0.0106 m/s. The retrieval result is slightly poor when the formula fitted by QPSI and QPSII data is applied to the Wave Mode data, which has RMSE with 2.04 m/s and bias with -1.16 m/s. This experiment uses the calibration constants after correction in cross-pol wind retrieval. Therefore, the calibration constants used here may have some differences with Ren. And the noise floor of QPSI, QPSII and Wave Mode is also slightly different. These may cause that the cross-pol retrieval method of Ren shows a different accuracy compared to the formula fitted in this paper.

4.3. Validation of PR Models using Testing Set

Preprints (www.preprints.org) | NOT PEER-REVIEWED | Posted: 9 May 2018 doi:10.20944/preprints201804.0223.v2

Peer-reviewed version available at Sensors 2018, 18, 1604; doi:10.3390/s18051604

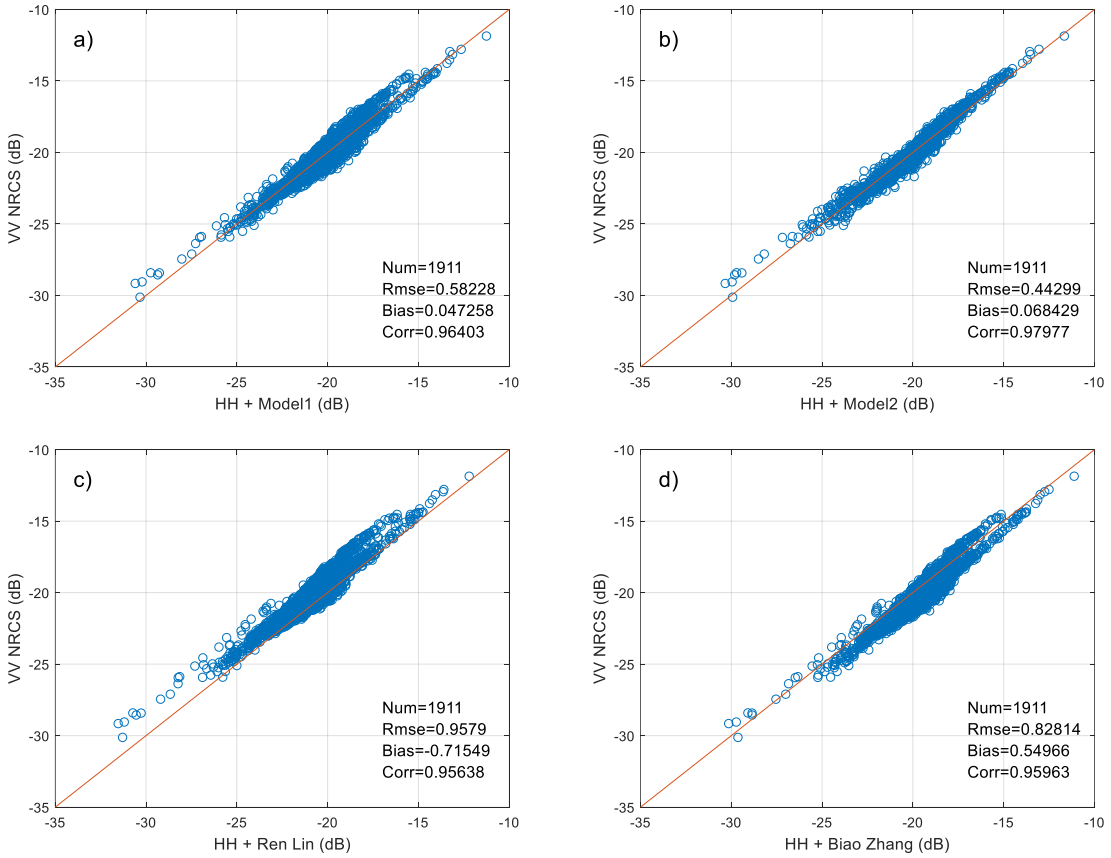

Figure 14. Comparison of four different PR models based on testing set

To evaluate the performance of two fitted PR models, we test the models in testing set and compare two models with different models in [27,45]. PR model proposed by Zhang in [27] is a function of incidence angle as well as wind speed and model fitted by Ren in [45] is dedicated to GF-3 QPSI and QPSII mode data.

Figures 14(a)-(d) illustrate the comparison of four PR models. The abscissa of figure is retrieved NRCS by PR model and the ordinate is NRCS from SAR image in VV polarization. Figures 14 also show the root-mean-square error (RMSE), bias and correlation coefficient for each model. It is shown that two models fitted in this study are in better agreement with Wave Mode data. The bias of Model1 and Model2 is much lower than two other models. And Model 2 which considers the influence of wind direction has a smaller RMSE (0.443dB) and larger correlation coefficient (0.98). In addition, Figure 14(c) shows the PR model proposed for GF-3 QPSI and QPSII mode cannot be well used in Wave Mode data. The retrieved NRCS is generally lower than observation. There may be two reasons for this result. First, the imaging bandwidth and system noise floor of two operating modes are different. These may affect the observation of NRCS. In addition, the PR model in Figure 14(c) is mainly fitted by data with incidence angles between 35°-38°, while PR models in this study are mainly applicable to data with incidence angles greater than 39°, due to the lack of data of small incidence angle.

5. Discussion

In this paper, we conduct a preliminary analysis of SAR images in Wave Mode for GF-3 satellite. 2779 GF-3 Wave Mode NRCS and wind vectors for the corresponding location are collected as training set and additional 1911 match-ups are as testing set. To reduce the effect of speckle noise and improve the matching precision of the data set, the NRCS is first sampled from 10m pixel spacing to 5km firstly, then the wind field interval is interpolated to 1h and the wind vectors of the center of each SAR image is calculated using bilinear interpolation.

A simple method for absolute radiometric calibration using ocean surface wind fields and CMOD4 is introduced and tested. Due to the linear relationship between NRCS and calibration constant, an estimator of calibration constant can be obtained by calculating the difference between the simulated NRCS and image value. Since the calibration constant given by China Centre for Resources Satellite Data and Application is only calculated by combing system bandwidth and antenna pattern, this experiment also verifies the constant using Amazon rainforest data. The result shows the obtained Amazon rainforest γ using estimated calibration constant is in good agreement with empirical γ. This normalized calibration method provides a more convenient and affordable way for future absolute radiometric calibration. It saves the expensive cost of calibration using corner reflector and can obtain an accurate calibration constant continuously.

The relationship between cross-pol images of Wave Mode and system noise floor, wind vectors and satellite geometry parameters is also investigated. The experiment indicates that the system noise floor of cross polarization is about -40dB. It is low enough and stable. There is a clear linear relationship between cross-pol NRCS and wind speeds in the case of ignoring noise floor effects, and the cross-pol NRCS is independent on incidence angle. As the wind speed increase, the cross-pol NRCS is more affected by azimuth angle. Therefore, it is necessary to consider the azimuth angle when retrieving high wind speed in the future.

The PR of Wave Mode is not only dependent on incidence angle but also modulated by the azimuth angle. Its first maximum corresponds to downwind direction, the second maximum in the upwind, and two minima appear in the crosswind direction. Moreover, when speed is lower than 10m/s, the PR presents a linear increase trend with wind speed in the downwind while it is independent on wind speed in other wind directions. Therefore, we fit two PR models which are suitable for large incidence angle using training set. The first is only dependent on incidence angle (Model 1) and the other one adds additional azimuth angle variable (Model 2). The results of two models on the testing set show that the PR models fitted in this paper are superior to models given in previous studies [24-28,45]. The Model 2 has higher polarization conversion accuracy than Model 1, with RMSE 0.443dB and correlation coefficient 0.98.

6. Conclusion

To date, GF-3 satellite only operates for less than two years and is still in the preliminary application stage. Since SAR images before February 2017 lack saturation coefficients and it cannot confirm whether the data is saturated or not, images used in this paper are all collected after March. Furthermore, as shown in the Table 2, the temporal and spatial distribution of SAR images are not uniform. Most data in the experiment is from the east Pacific Ocean near North America in September, October and November. The three-month data is mainly concentrated in beam 205 (41.7°). Therefore, the beam 205 is the main part of the data. The collected SAR images whose incidence angles are lower than 39° (lower than beam 200) are concentrated in March and April. They are all saturated and cannot be used. The reason for this may be inappropriate receiver gain setting at initial period of satellite operation. These lead to the non-uniformity distribution of incidence angle. In addition, we use the calibration constants after correction in cross-pol wind retrieval. And the noise floor of QPSI、QPII and Wave Mode is also slightly different. These may cause that cross-pol retrieval method of Ren shows a quite different accuracy compared to mine.

In the future work, we will collect more Wave Mode images which cover a wide range of incidence angles and wind speeds in high wind conditions. More system noise gain coefficient files will also be obtained to analyze the influence of noise floor on cross-pol wind speed retrieval. Moreover, we will further research the reasons for different polarization ratios under different operating modes to find a uniform PR model for GF-3 satellite.

Acknowledgments: The authors thank the National Satellite Ocean Application Service and China Centre for Resources Satellite Data and Application for providing GF-3 Wave Mode SAR data and calibration constants. And the wind fields are downloaded from ECMWF EAR-Interim http://apps.ecmwf.int/datasets/data/interim-full-daily/levtype=sfc/ for free. We would also like to thank Jingfeng Huang (Zhejiang University) and He Wang

(State Oceanic Administration) for our guidance, and to thank Lanqing Huang (Shanghai Jiao Tong University) and Lin Ren (State Oceanic Administration) for helpful discussions and suggestions.

Author Contributions: Lei Wang and Bing Han conceived and performed the experiments. Bin Lei and Chibiao Ding gave the experimental revisions. Lei Wang drafted the manuscript. And all authors contributed to the discussion and revising of the manuscript.

Conflicts of Interest: The authors declare no conflict of interest.

Appendix A

Table 6. Calibration Constants of Oher Beams

beams	constants
202	28.966
203	28.738
206	28.366
207	27.836
208	27.105
209	27.538
210	27.854
211	27.809

Appendix B

Table 7. Index of Abbreviations and Notations

Abbreviations	Full Name
GF-3	Gaofen-3
NOAA	National Oceanic and Atmospheric Administration
SAR	synthetic aperture radar
ECMWF	European Centre for Medium-Range Weather Forecasts
GMFs	empirical geophysical model functions
NRCS	normalized radar cross-section
PR	polarization ratio
NOC	Numerical Ocean Calibration
CAST	China Academy of Space Technology
SLC	single look complex
SNR	signal-to-noise ratio

References

1. Bergeron T, Bernier M, Chokmani K, et al. Wind Speed Estimation Using Polarimetric RADARSAT-2 Images: Finding the Best Polarization and Polarization Ratio[J]. IEEE Journal of Selected Topics in Applied Earth Observations & Remote Sensing, 2011, 4(4):896-904.
2. Zhang B, Perrie W, Vachon P W, et al. Ocean Vector Winds Retrieval From C-Band Fully Polarimetric SAR Measurements[J]. IEEE Transactions on Geoscience & Remote Sensing, 2012, 50(11):4252-4261.
3. Moon W M, Staples G, Kim D J, et al. RADARSAT-2 and Coastal Applications: Surface Wind, Waterline, and Intertidal Flat Roughness[J]. Proceedings of the IEEE, 2010, 98(5):800-815.
4. Yang X, Li X, Zheng Q, et al. Comparison of Ocean-Surface Winds Retrieved From QuikSCAT Scatterometer and Radarsat-1 SAR in Offshore Waters of the U.S. West Coast[J]. IEEE Geoscience & Remote Sensing Letters, 2010, 8(1):163-167.
5. Rivas M B, Stoffelen A, Zadelhoff G J V. The Benefit of HH and VV Polarizations in Retrieving Extreme Wind Speeds for an ASCAT-Type Scatterometer[J]. IEEE Transactions on Geoscience & Remote Sensing, 2014, 52(7):4273-4280.

6. Xu Q, Lin H, Li X, et al. Assessment of an analytical model for sea surface wind speed retrieval from spaceborne SAR[J]. International Journal of Remote Sensing, 2010, 31(4):993-1008.
7. Horstmann J, Koch W, Lehner S, et al. Wind retrieval over the ocean using synthetic aperture radar with C-band HH polarization[J]. IEEE Transactions on Geoscience & Remote Sensing, 2000, 38(5):2122-2131.
8. Plant W J. A two-scale model of short wind-generated waves and scatterometry[J]. Journal of Geophysical Research Oceans, 1986, 91(C9):10735–10749.
9. Romeiser R, Schmidt A, Alpers W. A three-scale composite surface model for the ocean wave–radar modulation transfer function[J]. Journal of Geophysical Research Oceans, 1994, 99(C5):9785-9801.
10. Romeiser R, Alpers W. An improved composite surface model for the radar backscattering cross section of the ocean surface: 2. Model response to surface roughness variations and the radar imaging of underwater bottom topography[J]. Journal of Geophysical Research Oceans, 1997, 102(C11):25251-25267.
11. Zou Q, He Y, Perrie W, et al. Wind-Vector Estimation for RADARSAT-1 SAR Images: Validation of Wind-Direction Estimates Based Upon Geometry Diversity[J]. IEEE Geoscience & Remote Sensing Letters, 2007, 4(1):176-180.
12. Escudero B, Diez A, Mart N A, et al. Scatterometer data interpretation: Estimation and validation of the transfer function CMOD4[J]. Journal of Geophysical Research Oceans, 1997, 102(C3):5767-5780.
13. Quilfen Y, Chapron B, Elfouhaily T, et al. Observation of tropical cyclones by high-resolution scatterometry. J. Geophys. Res. 103(C4), 7767-7786[J]. Journal of Geophysical Research Atmospheres, 1998, 103(C4):7,767-7,786.
14. Hersbach H, Stoffelen A, Haan S D. An improved C-band scatterometer ocean geophysical model function: CMOD5[J]. Journal of Geophysical Research Oceans, 2007, 112(C3).
15. Hersbach H. Comparison of C-Band Scatterometer CMOD5.N Equivalent Neutral Winds with ECMWF[J]. Journal of Atmospheric & Oceanic Technology, 2010, 27(4):721-736.
16. Monaldo F M, Thompson D R, Pichel W G, et al. A systematic comparison of QuikSCAT and SAR ocean surface wind speeds[J]. Geoscience & Remote Sensing IEEE Transactions on, 2004, 42(2):283-291.
17. Monaldo F, Thompson D. Implications of QuikSCAT and RADARSAT wind comparisons for SAR wind speed model functions[C]// Geoscience and Remote Sensing Symposium, 2002. IGARSS '02. 2002 IEEE International. IEEE, 2002:1881-1883 vol.3.
18. Yang X, Li X, Pichel W G, et al. Comparison of Ocean Surface Winds From ENVISAT ASAR, MetOp ASCAT Scatterometer, Buoy Measurements, and NOGAPS Model[J]. IEEE Transactions on Geoscience & Remote Sensing, 2011, 49(12):4743-4750.
19. Mouche A A, Hauser D, Daloze J F, et al. Dual-polarization measurements at C-band over the ocean: results from airborne radar observations and comparison with ENVISAT ASAR data[J]. IEEE Transactions on Geoscience & Remote Sensing, 2007, 43(4):753-769.
20. Rodrigues D F, Landau L, Junior A R T, et al. Sea Wind Extraction From RADARSAT-2 and Scatterometer Data Over the Gulf of Mexico[J]. IEEE Geoscience & Remote Sensing Letters, 2017, 14(7):1007-1011.
21. Monaldo F M, Thompson D R, Pichel W G, et al. Comparison of RADARSAT SAR-derived wind speeds with buoy and QuikSCAT measurements[C]// Geoscience and Remote Sensing Symposium, 2001. IGARSS '01. IEEE 2001 International. IEEE, 2001:1759-1760 vol.4.
22. Horstmann J, Koch W, Lehner S, et al. Coastal high-resolution wind fields retrieved from RADARSAT-1 ScanSAR[C]// Geoscience and Remote Sensing Symposium, 2001. IGARSS '01. IEEE 2001 International. IEEE, 2001:1747-1749 vol.4.
23. F. Monaldo, C. Jackson, X. Li, and W. G. Pichel, Preliminary evaluation of Sentinel-1A wind speed retrievals, IEEE [J]. Sel. Topics Appl. Earth Obs. Remote Sens., vol. 9, no. 6, pp. 2638–2642, Jun. 2016.
24. Thompson, D.R.; Elfouhaily, T.M.; Chapron, B. Polarization ratio for microwave backscattering from the ocean surface at low to moderate incidence angles. In Proceedings of the IEEE International Geoscience and Remote Sensing Symposium, Seattle,WA, USA, 6–10 July 1998; pp. 1671–1673.
25. Vachon, P.W.; Dobson, F.W. Wind retrieval from RADARSAT SAR images selection of a suitable C-band HH polarization wind retrieval model. Can. J. Remote Sens. 2000, 26, 2122–2131.
26. Monaldo F M, Thompson D R, Beal R C, et al. Comparison of SAR-derived wind speed with model predictions and ocean buoy measurements[J]. Geoscience & Remote Sensing IEEE Transactions on, 2002, 39(12):2587-2600.
27. Zhang, B.; Perrie, W.G.; He, Y.J. Wind speed retrieval from RADARSAT-2 quad-polarization images using a new polarization ratio model. J. Geophys. Res. 2011, 116, 1318–1323.

28. Mouche, A.A.; Hauser, D.; Daloze, J.F.; Guerin, C. Dual polarization measurements at C-band over the ocean: Results from airborne radar observations and comparison with ENVISAT ASAR data. IEEE Trans. Geosci. Remote Sens. 2005, 43, 753–769.
29. Wang H, Yang J, Mouche A, et al. GF-3 SAR Ocean Wind Retrieval: The First View and Preliminary Assessment[J]. Remote Sensing, 2017, 9(7):694.
30. Hwang P A, Zhang B, Perrie W. Depolarized radar return for breaking wave measurement and hurricane wind retrieval[J]. Geophysical Research Letters, 2010, 37(1):70-75.
31. Hwang P A, Zhang B, Toporkov J V, et al. Comparison of composite Bragg theory and quad-polarization radar backscatter from RADARSAT-2: With applications to wave breaking and high wind retrieval[J]. Journal of Geophysical Research Oceans, 2010, 115(C11):-.
32. Vachon P W, Wolfe J. C-Band Cross-Polarization Wind Speed Retrieval[J]. IEEE Geoscience & Remote Sensing Letters, 2011, 8(3):456-459.
33. Zhang B, Perrie W. Cross-Polarized Synthetic Aperture Radar: A New Potential Measurement Technique for Hurricanes[J]. Bulletin of the American Meteorological Society, 2011, 93(4):531-541.
34. Hwang P A, Perrie W, Zhang B. Cross-Polarization Radar Backscattering From the Ocean Surface and Its Dependence on Wind Velocity[J]. IEEE Geoscience & Remote Sensing Letters, 2014, 11(12):2188-2192.
35. Hwang P A, Stoffelen A, Zadelhoff G J V, et al. Cross-polarization geophysical model function for C-band radar backscattering from the ocean surface and wind speed retrieval[J]. Journal of Geophysical Research Oceans, 2015, 120(2):893-909.
36. Shen H, Perrie W, He Y, et al. Wind Speed Retrieval From VH Dual-Polarization RADARSAT-2 SAR Images[J]. IEEE Transactions on Geoscience & Remote Sensing, 2014, 52(9):5820-5826.
37. Horstmann J, Falchetti S, Wackerman C, et al. Tropical Cyclone Winds Retrieved From C-Band Cross-Polarized Synthetic Aperture Radar[J]. IEEE Transactions on Geoscience & Remote Sensing, 2015, 53(5):2887-2898.
38. Huang L, Liu B, Li X, et al. Technical Evaluation of Sentinel-1 IW Mode Cross-Pol Radar Backscattering from the Ocean Surface in Moderate Wind Condition[J]. Remote Sensing, 2017, 9(8):854.
39. Horstmann J, Lehner S. A new method for radiometric calibration of spaceborne SAR and its global monitoring[C]// Geoscience and Remote Sensing Symposium, 2002. IGARSS '02. 2002 IEEE International. IEEE, 2002:620-622 vol.1.
40. Stoffelen A. A Simple Method for Calibration of a Scatterometer over the Ocean[J]. Journal of Atmospheric & Oceanic Technology, 2010, 16(2):275-282.
41. Verspeek J, Stoffelen A, Verhoef A, et al. Improved ASCAT Wind Retrieval Using NWP Ocean Calibration[J]. IEEE Transactions on Geoscience & Remote Sensing, 2012, 50(7):2488-2494.
42. Zhu J, Dong X, Yun R. Calibration and validation of the HY-2 scatterometer backscatter measurements over ocean[J]. 2014(IGARSS):4382-4385.
43. Sun, J.L.; Yu, W.D.; Deng, Y.K. The SAR payload design and performance for the GF-3 mission. Sensors 2017,17, 2419
44. Shao W, Sheng Y, Sun J. Preliminary Assessment of Wind and Wave Retrieval from Chinese Gaofen-3 SAR Imagery.[J]. Sensors, 2017, 17(8).
45. Ren L, Yang J, Mouche A, et al. Preliminary Analysis of Chinese GF-3 SAR Quad-Polarization Measurements to Extract Winds in Each Polarization[J]. Remote Sensing, 2017, 9(12):1215.
46. Wang H, Wang J, Yang J et al. Empirical Algorithm for Significant Wave Height Retrieval from Wave Mode Data Provided by the Chinese Satellite Gaofen-3[J]. Remote Sensing, 2018, 10(3), 363.
47. Shao W, Yuan X, Sheng Y, et al. Development of Wind Speed Retrieval from Cross-Polarization Chinese Gaofen-3 Synthetic Aperture Radar in Typhoons[J]. Sensors, 2018, 18(2).
48. Chang Y, Li P, Yang J, et al. Polarimetric Calibration and Quality Assessment of the GF-3 Satellite Images[J]. Sensors, 2018, 18(2):403.
49. Horstmann J, Schiller H, Schulz-Stellenfleth J, et al. Global wind speed retrieval from SAR[J]. Geoscience & Remote Sensing IEEE Transactions on, 2003, 41(10):2277-2286.
50. ECMWF ERA-Interim Daily. Available online: http://apps.ecmwf.int/datasets/data/interim-full-daily/levtype=sfc/
51. Birrer I J, Bracalente E M, Dome G J, et al. σ° Signature of the Amazon Rain Forest Obtained from the Seasat Scatterometer[J]. IEEE Transactions on Geoscience & Remote Sensing, 2007, GE-20(1):11-17.

601 52. Hawkins R, Attema E, Crapolicchio R, et al. Stability of Amazon Backscatter at C-Band: Spaceborne Results
602 from ERS-1/2 and RADARSAT-1.[J]. 1999, 450:99.
603 53. Shao W, Sun J, Guan C, et al. A Method for Sea Surface Wind Field Retrieval from SAR Image Mode Data[J].
604 Journal of Ocean University of China, 2014, 13(2):198-204.
605 54. Raney R K, Freeman T, Hawkins R W, et al. A plea for radar brightness[C]// Geoscience and Remote Sensing
606 Symposium, 1994. IGARSS '94. Surface and Atmospheric Remote Sensing: Technologies, Data Analysis and
607 Interpretation. International. IEEE Xplore, 1994:1090-1092 vol.2.

608